Stratocumulus processing of gases and cloud condensation nuclei 2. Chemistry sensitivity analysis

Yiping Zhang[1] and Sonia M. Kreidenweis

Department of Atmospheric Science, Colorado State University, Fort Collins

Graham Feingold

Cooperative Institute for Research in the Atmosphere / NOAA Environmental Technology Laboratory, Boulder Colorado

Abstract. A trajectory ensemble model (TEM) is used to investigate aqueous processing of gases and cloud condensation nuclei (CCN) in the boundary layer. The coupled aqueous chemistry/cloud microphysics model driven by a set of boundary layer parcel trajectories derived from a large eddy simulation is used to study the effects of variations in the initial chemical fields and initial aerosol number concentration on chemical heterogeneity, and the broadening of CCN and drop spectra. The differences in the overall fractional conversion between the TEM and a single parcel experiencing mean conditions in a stratocumulus-capped marine boundary layer are also investigated. Results show that the O_3 oxidation rate is larger than the H_2O_2 oxidation rate in the base case, whereas the volume-mean pH might suggest that H_2O_2 oxidation dominates. Aqueous chemistry contributes to broadening of the drop size distribution, but the magnitude of the broadening also depends on initial chemical conditions. Sensitivity tests show that the H_2O_2 oxidation adds sulfate mass evenly and continuously across the particle sizes, while the O_3 oxidation adds sulfate mass near the mode of the CCN spectrum over a relatively short time. In cases where more mass is added onto large particles in the tail of the initial CCN spectrum, the broadening of the drop spectrum is most evident, and may even trigger the collision–coalescence process and drizzle formation in stratocumulus clouds.

1. Introduction

Marine stratocumulus clouds play an important role in the global radiation budget primarily because of their large areal extent and temporal persistence, and because they may be sensitive to anthropogenic influences and strongly influence the planetary albedo [e.g., *Nakajima et al.*, 1991; *Randall et al.*, 1984; *Slingo*, 1990]. Stratocumulus clouds serve as a medium for in-cloud sulfate production, which in turn, modifies the cloud condensation nuclei (CCN) spectra and cloud optical properties, thus influencing global climate. Observations and model studies in the marine boundary layer described in the literature show strong evidence of bimodal aerosol spectra due to cloud processing of aerosol via aqueous chemistry [*Bower and Choularton*, 1993; *Hegg et al.*, 1996; *Hoppel and Frick*, 1990; *Hoppel et al.*, 1994]. *Bower and Choularton* [1993] studied cloud processing in a hill cap cloud and concluded that small CCN particles activate much more readily after cloud processing and that the droplet effective radii are lowered in the secondary cloud. On the other hand, *Feingold et al.* [1998] (henceforth Part I), showed that in cases where processing does not enhance the number of cloud drops significantly, drizzle formation may

be enhanced. This occurs because some of the processed particles are larger, thereby enabling the formation of larger drops.

It has also been realized by observations and model studies that clouds are not chemically homogeneous and that the chemical heterogeneity across the droplet size spectrum has consequences for aqueous chemistry [*Daum et al.* 1984; *Hegg and Larson*, 1990; *Noone et al.*, 1988; *Gurciullo and Pandis*, 1997; *Pandis et al.*, 1990; *Twohy et al.*, 1989]. In particular, the chemical conversion rates estimated for bulk solutions can be substantially different from those computed for a size-resolved droplet spectrum [*Gurciullo and Pandis*, 1997]. While many of the previous studies used a single parcel model to examine chemical heterogeneity, aqueous sulfate production, and modification of aerosol spectra, the interaction between microphysics/chemistry and dynamics was not properly addressed, as discussed in Part I and by *Feingold et al.* [1996]. It is also difficult to compare the results from a parcel model with field measurements because a single average parcel does not represent the variability associated with many air parcels experiencing different dynamical, microphysical, and chemical processes. For example, *Bower and Choularton* [1993] used a single parcel model to examine modification of the CCN spectrum following a cloud cycle and its consequence for secondary cloud formation, but the parcel dynamics were prescribed ad hoc.

In an attempt to describe the variability that air parcels are likely to encounter in the boundary layer, this work employs a set of 500 trajectories recorded from a large eddy simulation

---

[1]Now at National Center for Atmospheric Research, Boulder, Colorado.

(LES), as described by *Stevens et al.* [1996], to drive a coupled microphysics/chemistry parcel model, called a trajectory ensemble model (TEM). The trajectories represent parcel motions through the cloudy boundary layer and include a statistical description of the time that parcels spend in cloud and their liquid water content histories along those trajectories. Thus the main advantage of the TEM is that it represents the impacts of variable in-cloud transit times and repeated cycling through cloud. Here we elect to use it to study the interaction of chemistry and cloud and the effects of aqueous chemistry on the modification of CCN spectra and drop spectra.

The TEM framework is not without its drawbacks, as discussed at length by *Stevens et al.* [1996] and in Part I. For example, the TEM forces a decoupling of the microphysics/chemistry and dynamics, it gives poor resolution of the cloud-top region where turbulent motions are not well resolved by the LES, and within the context of this study, the fact that there is no communication of information between parcels is expected to have some influence on the degree of processing of CCN and gases (see section 4.5). In spite of this, much can be gleaned from this approach, provided that the TEM assumptions and their implications for specific processes are borne in mind.

In the following sections the TEM is used to explore a number of specific issues from an ensemble point of view: (1) the effect of different initial chemical fields on S(IV) depletion and S(VI) production; (2) the chemical heterogeneity of cloud water pH and S(VI) concentration across the drop spectrum; (3) the relative importance of contributions of O_3 and H_2O_2 to the overall oxidation rate; (4) the impact of different oxidation pathways on the shape of CCN and drop spectra and possible implications for drizzle production; and (5) the use of approximate conversion rates and time constants to represent the ensemble mean processing by clouds.

2. TEM Description

A set of 500 trajectories is chosen from a large eddy simulation of a stratocumulus-capped marine boundary layer, as described more fully by *Stevens et al.* [1996] and in Part I. The LES is initiated with a case study based on the dynamics of the First International Satellite Cloud Climatology Project (ISCCP) Regional Experiment (FIRE) July 7, 1987, event held off the coast of California [*Betts and Boers,* 1990]. The simulated July 7 case features little or no precipitation. Because there were no data available for this case for the aerosol chemical composition, pH of the cloud water, or gaseous species concentrations, the approach taken here is to consider the LES dynamics as representative of the stratocumulus-capped marine boundary layer and use the model as a source of parcel trajectories for the TEM. Then within the TEM framework, the assumed initial concentrations are varied to study their impact on stratocumulus processing of gases and CCN spectra.

During the course of the LES run, 500 parcels are released within the boundary layer (below cloud and between 200 and 450 m) and the essential fields (position, vertical velocity, pressure, liquid-water potential temperature, and total water mass mixing ratio) are recorded every 2 s, the LES model time step, for a period of 1 hour. Information is interpolated trilinearly from adjacent grid points ($\Delta z = 25$ m, $\Delta x = \Delta y = 50$

m) as described by *Stevens et al.* [1996]. These data and their prescribed tendencies are used to drive 500 individual Lagrangian parcels. Each Lagrangian parcel includes microphysical and chemical components, which will be discussed below.

2.1. Microphysics

The initial aerosol is assumed to have a uniform chemical composition of ammonium sulfate. For simplicity, we define the aerosol size spectrum by five logarithmically spaced discrete sizes, but these can be extended to as many sizes as needed. Sensitivity tests using 10 sizes and 25 sizes have been performed and have produced similar S(IV) to S(VI) conversion. The solute mass in each size category is carried as ammonium ion mass and sulfate ion mass independently, to allow variations in the ratio of ammonium to sulfate as chemical reactions proceed in a parcel cycling through cloud. The condensational growth of these particles is solved on a moving mass grid; coagulation and collision – coalescence processes are not modeled. (For a discussion of collision – coalescence processing of CCN, see *Feingold et al.* [1996].) Independent variables temperature T, droplet radius r, and water vapor mixing ratio r_v are integrated using the ordinary differential equation solver VODE [*Brown et al.*, 1989]. The parcels are not assumed to be adiabatic; instead, the tendencies of nonadiabatic liquid water potential temperature and total water mass mixing ratio, which depend on calculations in the LES host model, are prescribed from the trajectories to determine the time rate of change of T, r_v, and liquid water mixing ratio r_l.

The supersaturation field which drives droplet growth is then calculated from T and r_v at the current time step. Droplet growth is solved following *Pruppacher and Klett* [1978], in which the water activity of the multicomponent solution inside the growth equation is calculated using the Zdanovskii-Stokes-Robinson (ZSR) relation [*Sangster and Lenzi*, 1974]. Water activity data for the binary solutions are obtained from *Chen* [1994] and *Tang and Munkelwitz* [1994]. For purposes of computing water activity, the solution is assumed to be a mixture of ammonium sulfate and ammonium bisulfate when the ammonium to sulfate molar ratio is between 1 and 2; and the solution is assumed to be a mixture of ammonium bisulfate and sulfuric acid when the molar ratio of ammonium to sulfate is between 0 and 1. Additional details of the microphysics used in the TEM can be found in Part I and *Feingold and Heymsfield* [1992].

2.2. Chemistry

In this application, each parcel is treated as a closed system, with no gas phase sources or replenishment so as to investigate the chemistry behavior in a controlled dynamical framework. We assume a parcel will keep its identity in the boundary layer until five or six characteristic eddy mixing times have elapsed, as discussed in Part I. Thus allowing no mixing of chemistry is probably reasonable during a 1 hour simulation. Possible impacts of this assumption are explored in section 4.5.

The aerosol composition is restricted to ammonium and sulfate species. Relevant sulfur chemistry is simulated, including the dissolution and reaction of SO_2, O_3, H_2O_2, and NH_3. Instead of assuming instantaneous equilibrium between the gas and aqueous phases, the mass-transfer rate of species

Table 1. Chemical Reactions Included in the TEM

Equilibrium Reaction	Equilibrium Constant, M or M atm^{-1}	$-\Delta H/R$, K	Reference
(1) $SO_2(g) \Leftrightarrow SO_2 \bullet H_2O$	1.23	3120	*Smith and Martell* [1976]
(2) $SO_2 \bullet H_2O \Leftrightarrow HSO_3^- + H^+$	1.23×10^{-2}	1960	*Smith and Martell* [1976]
(3) $HSO_3^- \Leftrightarrow SO_3^{2-} + H^+$	6.61×10^{-8}	1500	*Smith and Martell* [1976]
(4) $H_2O_2(g) \Leftrightarrow H_2O_2(aq)$	7.45×10^4	6620	*Lind and Kok* [1986]
(5) $O_3(g) \Leftrightarrow O_3(aq)$	1.13×10^{-2}	2300	*Kozac-Channing and Heltz* [1983]
(6) $NH_3(g) \Leftrightarrow NH_4OH(aq)$	75	3400	*Hales and Drewes* [1979]
(7) $NH_4OH(aq) \Leftrightarrow NH_4^+ + OH^-$	1.75×10^{-5}	-450	*Smith and Martell* [1976]
(8) $H_2SO_4(aq) \Leftrightarrow HSO_4^- + H^+$	1000		*Perrin* [1982]
(9) $HSO_4^- \Leftrightarrow SO_4^{2-} + H^+$	1.02×10^{-2}	2720	*Smith and Martell* [1976]
(10) $H_2O \Leftrightarrow H^+ + OH^-$	1.0×10^{-14}	-6710	*Smith and Martell* [1976]
Aqueous Phase Reactions	Rate Coefficient, M^n s^{-1}	$-E/R$, K	Reference
(11) $S(IV) + H_2O_2 \rightarrow S(VI) + H_2O$	7.45×10^7	-4751	*Hoffmann and Calvert* [1985]
(12) $S(IV) + O_3 \rightarrow S(VI) + O_2$	2.4×10^4		
	3.7×10^5	-5533	
	1.5×10^9	-5280	*Hoffmann and Calvert* [1985]

The temperature dependence is represented by $K(T) = K_{298} \exp\left[\dfrac{-\Delta H}{R}\left(\dfrac{1}{298} - \dfrac{1}{T}\right)\right]$ for the equilibrium constant, and $k = k_{298} \exp\left[\dfrac{-E}{R}\left(\dfrac{1}{298} - \dfrac{1}{T}\right)\right]$ for the rate coefficient.

between phases is calculated, as in the work by *Pandis and Seinfeld* [1989]. The mass-transfer coefficients are the same among species, since we assume all species have the same diffusivity. This assumption has only a minor effect on the mass-transfer rates and little effect on the overall chemistry output. The mass-transfer coefficients also depend inversely on drop size, so that the gas phase species equilibrate more quickly with small drops than with large ones.

In each size category the concentrations of gas phase SO_2, O_3, H_2O_2, NH_3, and of aqueous phase $S(IV)$, $S(VI)$, $O_3(aq)$, $H_2O_2(aq)$ and $N(III)$ are also integrated using VODE. The general expressions for the time rate of change of concentrations in the aqueous and gas phase can be found in the work by *Lelieveld and Crutzen* [1991] and *Pandis and Seinfeld* [1989]. The electroneutrality equation includes the positive ions H^+, NH_4^+ and the negative ions OH^-, HSO_4^-, SO_4^{2-}, HSO_3^-, and SO_3^{2-}. The $S(IV)$ to $S(VI)$ conversion is via the O_3 and H_2O_2 oxidation pathways [*Hoffmann and Calvert*, 1985]. The chemical reactions and equilibrium equations are listed in Table 1.

When sufficient cloud water is present ($r_l > 1 \times 10^{-6}$ g g^{-1}air), chemistry calculations are performed on those droplet categories with ionic strength < 2 M, which allows for chemistry in haze particles [*Seinfeld*, 1986]. If the ionic strengths for all five size categories are higher than 2 M, chemistry calculations are terminated, and only microphysical processes are solved for.

3. Results

3.1. Initial Conditions

The trajectory set and the initial aerosol size distribution and composition are identical to those used in Part I. The aerosol population is assumed to have a lognormal distribution with geometric mean radius r_g=0.05 µm, total

number concentration N=50 cm^{-3}, and geometric standard deviation σ_g=1.8, and consists of particles with dry radii of 0.011 µm, 0.035 µm, 0.11 µm, 0.35 µm, and 1.1 µm. The corresponding initial dry sulfate ion mass concentrations in each size category are ~0.005 ppt, 2.3 ppt, 21 ppt, 4.1 ppt, and 0.02 ppt, respectively. The initial gas phase chemical fields are different from those used in Part I for polluted marine air. We choose case 5 from *Bower and Choularton* [1993] as our base case, to simulate a moderately polluted marine environment. The $S(IV)$ to $S(VI)$ conversion in the base case is H_2O_2 limited, where oxidation by O_3 and H_2O_2 both play a role in the $S(IV)$ to $S(VI)$ conversion. In the sensitivity cases discussed below, we simulate a SO_2 limited case, where oxidation by H_2O_2 dominates the $S(IV)$ to $S(VI)$ conversion, and we also simulate a case where the initial ratio $NH_3/SO_2 > 2$, in which oxidation by O_3 boosts and dominates the overall $S(IV)$ to $S(VI)$ conversion. The initial values of gas phase SO_2, H_2O_2, and O_3 concentrations for the base case and the sensitivity simulations are in agreement with observations and other model studies [*Bower and Choularton*, 1993; *Macdonald et al.*, 1995; *Müller and Mauersberger*, 1994]. The initial aerosol and gas phase concentrations are shown in Table 2.

3.2. pH Calculations and Drop Spectra

Droplets of different sizes experience different gas mass-transfer rates, chemical conversion rates, water growth, and water evaporation rates. Droplets in different parcels also experience different histories (supersaturations, in-cloud residence times, liquid water contents). These differences lead to chemical heterogeneities in the drop population. Some previous modeling studies have assumed a size-dependent composition for the initial aerosol population. Those simulations suggest that larger drops tend to have higher pH compared to small drops, mainly because the composition of

Table 2. Initial Chemical and Aerosol Fields for the TEM

	Base Case (H₂O₂ Limited)	Sensitivity Test 1 (SO₂ Limited)	Sensitivity Test 2 (NH₃/SO₂>2)	Sensitivity Test 3 (Initial CCN=150 cm⁻³)
SO_2, ppb	2	2	2	2
H_2O_2, ppb	0.3	2.5	0.3	0.3
O_3, ppb	30	30	30	30
NH_3, ppb	1	1	4.05	1
HNO_3, ppb	0	0	0	0
Aerosol	$(NH_4)_2SO_4$, lognormal distribution, N_{CCN} = 50 cm⁻³, r_g = 0.05 μm, σ_g = 1.8	Same as base case	Same as base case	N_{CCN} = 150 cm⁻³; other parameters are same as base case

	Size category				
	1	2	3	4	5
Initial r, μm	0.011	0.035	0.11	0.35	1.1
Number, cm⁻³	2.5	33.26	9.54	0.06	7.9×10^{-6}
Initial mass, g	1×10^{-17}	3.16×10^{-16}	1×10^{-14}	3.16×10^{-13}	1×10^{-11}

the particles on which those larger drops formed is more basic (e.g., sea salt) [*Hegg and Larson*, 1990; *Hegg et al.*, 1996; *Gurciullo and Pandis*, 1997]. In contrast, here we assume a size-independent initial aerosol composition. Thus pH differences between larger and smaller drops are due to the contributions from dilution (droplet diffusional growth) or evaporation, size-dependent gas uptake and chemical conversion, and parcel in-cloud time history.

3.2.1. Microphysics only. To separate the contributions from microphysical and chemical processes to the pH inhomogeneity among the droplets, we perform a control run which simulates only the effect of microphysical processes on pH by setting to zero all the chemical reaction rates and gas and aqueous phase exchange of chemical species. However, the incomplete dissociation of N(III) and S(VI) in the aqueous phase is computed.

The computed pH values averaged over the last 10 min of the control run simulation are plotted as a function of drop size in different cloudy layers in Figure 1a. The cloud top is slightly above 735 m, and the cloud base is slightly below 510 m in this simulation (Figure 2a); therefore all layer averages are taken in cloud. To ensure collection of a sufficient sample for the large droplets, we sample to a drop-size grid that triples the mass from one grid point to the next and covers the range from 2 μm to 37 μm in nine size bins. Those drops with radius greater than 37 μm are sampled to the largest sampling bin, from 25 to 37 μm. The pH values are calculated as liquid water-weighted mean values ($-\log_{10}$ [Σr_{li}[H⁺]$_i$ / Σr_{li}]) over the last 10 min of the simulation, and over each 75 m height interval, and plotted at the midpoint of each sampling bin. Thus each data point represents an average pertaining to those drops that fall into the given size and height range. Only averages having mean r_l > 0.9×10-11 g g⁻¹ are included. The average S(VI) concentration (proportional to solution molarity) for each size interval is plotted on the right axis in Figure 1a. In Figure 1b the average dr_l/dr (i.e., the total water collected in that size interval divided by the number of parcels sampled, and the bin width) is plotted against drop size. Because the control run only simulates microphysical processes, Figures 1a and 1b demonstrate the effects of droplet growth, evaporation, and microphysical environment on the pH calculation and drop spectra.

Figure 1a suggests that the pH and solute concentrations are inversely related and that the S(VI) concentration as a function of drop size has a U shape. These same characteristics have been pointed out in previous single parcel modeling studies [e.g., *Pandis et al.*, 1990; *Roeloefs*, 1992]. In a single closed parcel, like that used by *Pandis et al.* [1990], the size ordering of the CCN as they grow into droplets remains the same if the CCN have the same composition. That is, drops formed on small particles cannot grow larger than drops formed on large particles. The characteristic U shape is thus produced by highly dilute small particles, located near the minimum in concentration, and less dilute larger droplets forming the right branch. The left branch is composed of never-activated and/or evaporating droplets.

Although the same ordering is found among the drops formed within individual parcels in the TEM, the ordering disappears when a composite is made of all these parcels, all experiencing different histories and trajectories through the cloud layer over which they have been averaged. To elucidate the CCN-drop relationships forming this average, Figure 3 shows a scatterplot of all of the droplets contributing to Figure 1a, sorted by the CCN size category upon which they formed. Each CCN category describes a path in [S(VI)]-drop radius space that follows the dilution of that size particle as the droplet grows by water mass addition. It is clear from Figure 3 that once this averaging is performed there is no longer a unique ordering between drop size and CCN size, e.g., an 8 μm drop can contain a CCN particle from categories 2, 3, 4, or 5. The averaged S(VI) concentration at any drop size reflects the relative contributions from CCN in each category. These relative contributions are shown as histograms in Figure 4, from which we see that the small CCN contribute primarily to small drop sizes and that large drops are formed primarily on large CCN.

The mode of the distribution (drop bin with midpoint near 7.3 μm), however, contains approximately equal numbers of category 2, 3, and 4 CCN. The drops in categories 2 and 3 that have grown this large are more dilute, by several orders of magnitude, than those from category 4. The averaged result is that a minimum in S(VI) concentration is found in these midsized drops. It is worth noting that in Figure 1a all drops formed on category 1, 2, and 3 CCN are activated; that is, they
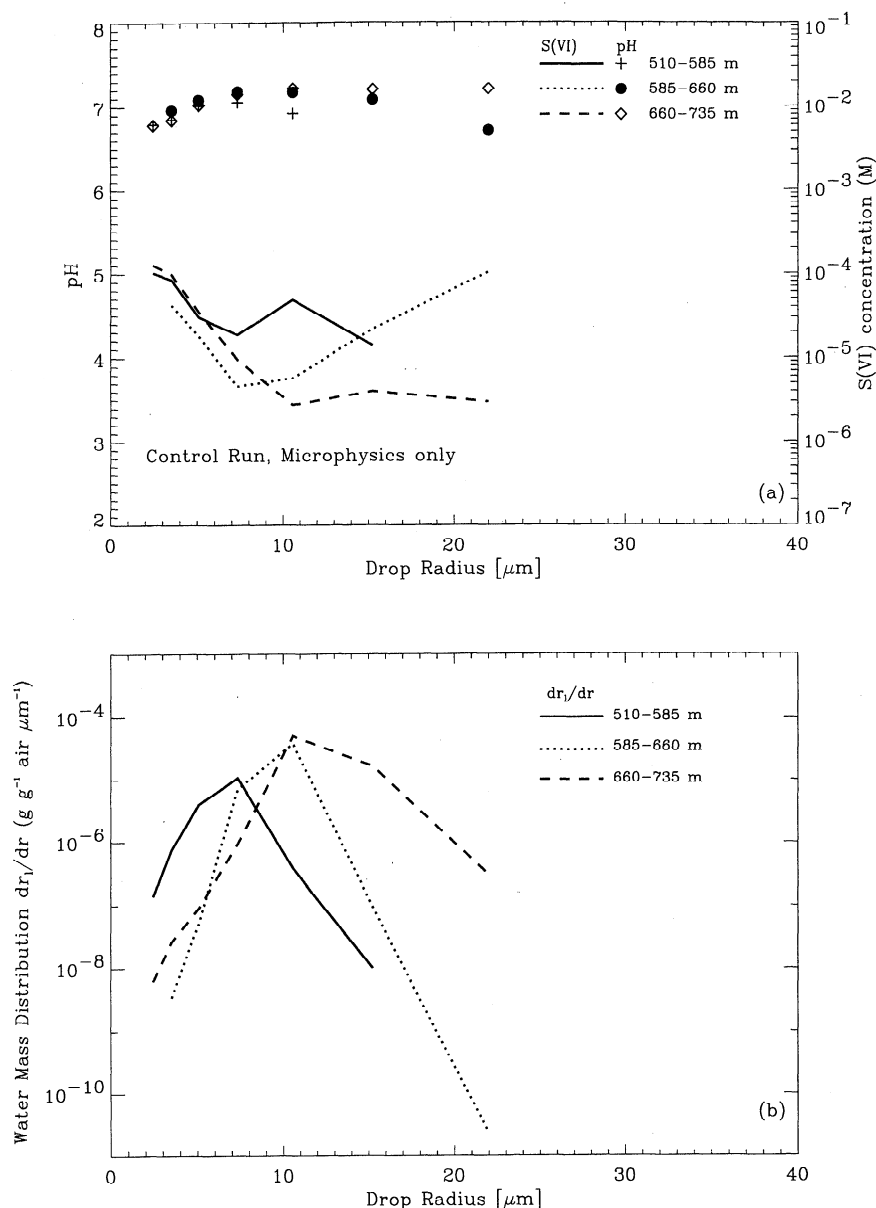
Figure 1. (a) The calculated liquid water-weighted mean pH as a function of drop radius over the last 10 min of the control run. The right-hand coordinate is S(VI) concentration in each size interval. (b) The water mass distribution dr_l/dr. Calculations are performed for mass tripling sampling intervals at three different 75 m height intervals (in cloud) as indicated. The lines are for dr_l/dr or S(VI) concentration in each drop size interval, and the symbols are for pH values in each size interval.

have grown well past their critical radius (r_c); drops smaller than 7.3 μm that contain category 4 CCN are below their critical size; and all drops formed on category 5 CCN are unactivated $(r_c = 41$ μm). Therefore most of the drops contributing to the extreme left branch of the U are, in fact, activated droplets and not haze particles.

The drop spectra shown in Figure 1b are broader than the nearly monodisperse spectra predicted by a single adiabatic updraft model initialized with a unimodal, uniform composition aerosol. This broadening is due to a number of factors: (1) some broadening results from the 75 m height bin used in the averaging; in the mean, spectra near the base of a height bin tend to have smaller droplets, while those at the

top of the height bin have larger drops (Figure 2b) so that the averaged spectrum is broader than the individual component spectra; (2) the presence of parcels with fewer CCN categories growing to cloud droplet sizes will have the potential to broaden the tail of the drop spectra, since the less numerous drops can grow to larger sizes; (3) another source of broadening is due to the variations in individual parcel histories, including supersaturation fluctuations. *Mazin* [1968] showed that turbulent mixing of spectra that have experienced different growth histories and supersaturation fluctuations causes spectral broadening. On the other hand, *Korolev* [1995] showed that even a single parcel that is cycled through cloud numerous times can develop spectral
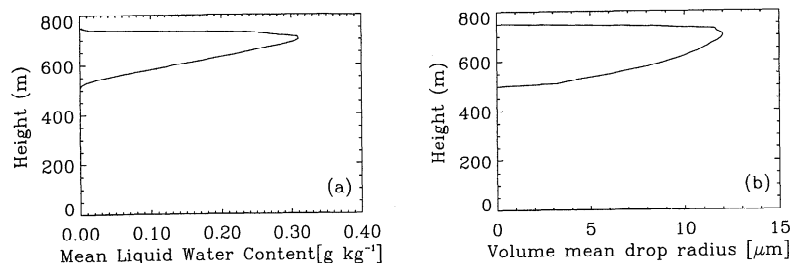
Figure 2. The vertical profile of (a) mean r_l and (b) volume mean cloud drop radius for the base case.

broadening as a result of the irreversibility of the droplet growth equation in the presence of solute and curvature effects.

3.2.2. Microphysics and chemistry. We now look at the combined microphysical and chemical effects in the base case, including gas exchange and reactions, on the chemical heterogeneity of cloud drops. The total r_l for the base case is approximately the same as that in the control run (less than 2% difference). Figure 5 is similar to Figure 1 but considers both microphysics and chemistry (base case). The cloud water pH and S(VI) concentration have a slight height dependence (Figure 5a). For the combined chemistry / microphysics run, at smaller drop sizes, the lowest cloud layer always has some newly introduced parcels with higher pH; parcels just entering the cloud for the first time during this period initially have high NH_3 gas concentrations and contribute to the higher pH values in the lowest cloudy layer. As parcels penetrate farther into cloud and S(IV) to S(VI) conversion continues, the pH decreases.

In each cloud layer the cloud water pH generally increases with drop size to a maximum and then decreases with further increases in size. The pH peak has a tendency to shift to larger drop sizes at higher levels in cloud, and the S(VI) concentration U shape tends to shift to a larger drop size and to have a lower minimum closer to cloud top, in agreement

with the control run results (Figure 1). Note that the pH peak for each layer has shifted to the next sampling interval, compared with the radius at the pH peak in the control run. This is because chemical reactions are faster at the larger r_l, which counters the effects of dilution and lowers the pH. In the base case the S(VI) concentrations have increased by 1 or 2 orders of magnitude over those in the control run, due to aqueous chemistry. Drop spectra for the base case are shown in Figure 5b and are seen to be similar to those from the control run but with a tendency for higher concentrations of large drops in the control run. In the base case, many of the parcels sampled during the last 10 min had prior sojourns into cloud, during which sulfate mass was added to particles dilute enough to participate in heterogeneous chemistry. This mass addition is in some cases sufficient to enable more drops to grow to radii > 2 μm than in the control run. The base case drop spectra therefore have higher drop concentrations, more competition for available vapor, and narrower spectra than their control case counterparts.

3.3. N(III)/S(VI) Ratios

The snapshots of the computed N(III)/S(VI) ratios, where N(III)=NH_3(aq)+NH_4^+, and S(VI)=H_2SO_4(aq)+SO_4^{2-}+HSO_4^-, for the drop-size range from 8 to 12 μm, are plotted at different
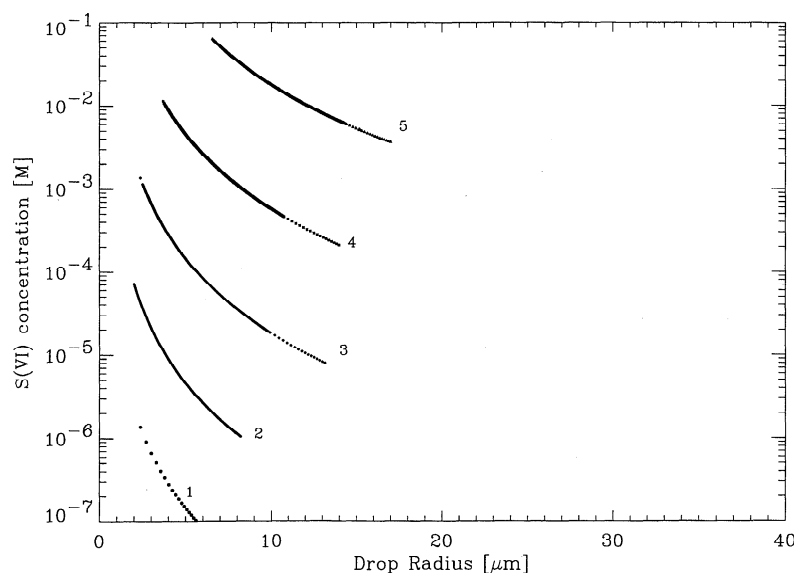

Figure 3. Scatterplot of [S(VI)] versus size for drops contributing to the 510-585 m layer in Figure 1, sorted by CCN category (1 through 5) on which they were formed.
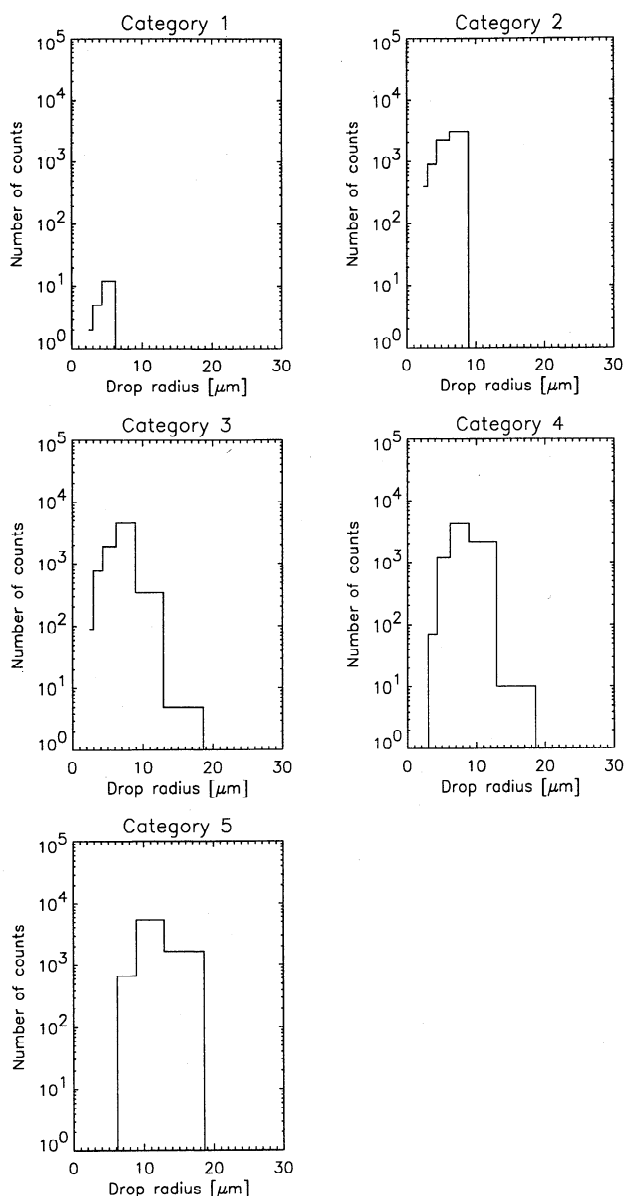
Figure 4. Histograms of frequency of occurrence of CCN category within various drop sizes.

times for three different cloudy layer intervals in Figure 6. At a specific time, values are the molar ratios of average N(III) to average S(VI) in each height interval, so that one data point represents all parcels found in that height interval. Data points with less than 10 parcels found in the height interval are filtered out. The liquid water-weighted pH values are plotted on the right axis. Initially, the N(III)/S(VI) ratios are greater than 2 because gaseous NH3 dissolves into the aqueous phase more quickly than S(IV) is converted to S(VI). After some time has elapsed, these ratios tend to be between 1.6 and 2. In the lowest cloudy layer, ratios greater than 2 and correspondingly high pH values appear periodically, showing the strong signals of parcels entering cloud for the first time. Generally, N(III)/S(VI) ratios are the largest and have the highest variability in the lowest cloudy layer. This is in part because all the parcels are originally released below cloud between 200 m and 450 m. When parcels enter cloud, NH3 gas

quickly dissolves into the aqueous phase and maintains the O3 oxidation for several minutes; as S(IV) to S(VI) conversion proceeds in parcels staying in cloud, producing more S(VI) in the aqueous phase, the ratios of N(III) to S(VI) decrease with height. The lowest cloudy layer also has the lowest liquid water content, which restricts the chemical conversions that tend to lower cloud water pH and decrease N(III) to S(VI) ratios. In each layer the decrease in N(III)/S(VI) ratios generally corresponds to the decrease in the pH values.

The raw unaveraged NH_4^+/SO_4^{2-} ratios in each particle size category are plotted as functions of dry particle radius at three different times, and three different 75 m height intervals below the cloud, as shown in Figure 7. The particles that have never been sufficiently diluted to permit chemistry to proceed have NH_4^+/SO_4^{2-} ratios of 2. In most parcels the smallest particle size category 1 never participates in the SO2 oxidation chemistry. There is some conversion performed on these particles in some parcels, so that the molar ratios are below 2; however, the slow chemistry on these haze particles with negligible liquid water content has little effect on the addition of S(VI) mass or change of particle size. One parcel at 20 min between 435 and 510 m, three parcels at 60 min between 360 and 435 m, and two parcels at 50 min between 285 and 360 m experience conditions such that droplets formed on all categories are sufficiently dilute for heterogeneous chemistry to proceed. These parcels produce the lowest NH_4^+/SO_4^{2-} ratio in the smallest size category. Generally, the NH_4^+/SO_4^{2-} ratios in category 2 and 3 particles have large variability and the lowest values, since the added sulfate mass has a more prominent effect on the composition of small particles than on that of large particles. In the base case, particles that have grown to 0.2 and 0.3 μm radius are those for which aqueous phase chemistry has added the most sulfate mass or produced the most pronounced effect on composition and size. In particular, Figure 7 suggests that processed particles in the size range 0.1-1 μm are more acidic than larger particles and those smaller particles that have not been processed in cloud.

3.4. Oxidation Rates and Gas Depletion Rates

From the above discussion of the control run and the base case, aqueous chemistry has an impact on chemical heterogeneity. Aqueous chemistry also exerts a measurable influence on CCN and drop spectra, and this will be discussed in sensitivity tests in section 4. Oxidation by H2O2 and O3 pathways contributes to the aqueous sulfur-to-sulfate conversion. It is of interest to examine the relative importance of these two pathways, which depend on the initial chemical species concentration and cloud water pH.

Figure 8a shows the time when each of the 500 parcels first enters the cloud. It is interesting to note that there are almost always new parcels entering the cloud, with only some small gaps in time indicating the absence of parcels with first entries into cloud. In Figures 8b-8d the oxidation rates contributed by the H2O2 and O3 pathways in the base case are plotted against time for parcels 2, 39, and 232, chosen randomly from parcels entering cloud during the first 10 min, between 10 and 50 min, and during the last 10 min, respectively. The times corresponding to these three parcels are also marked in Figure 8a with solid diamonds. The oxidation rate for each pathway is the sum of the contributions from each droplet size category. The common
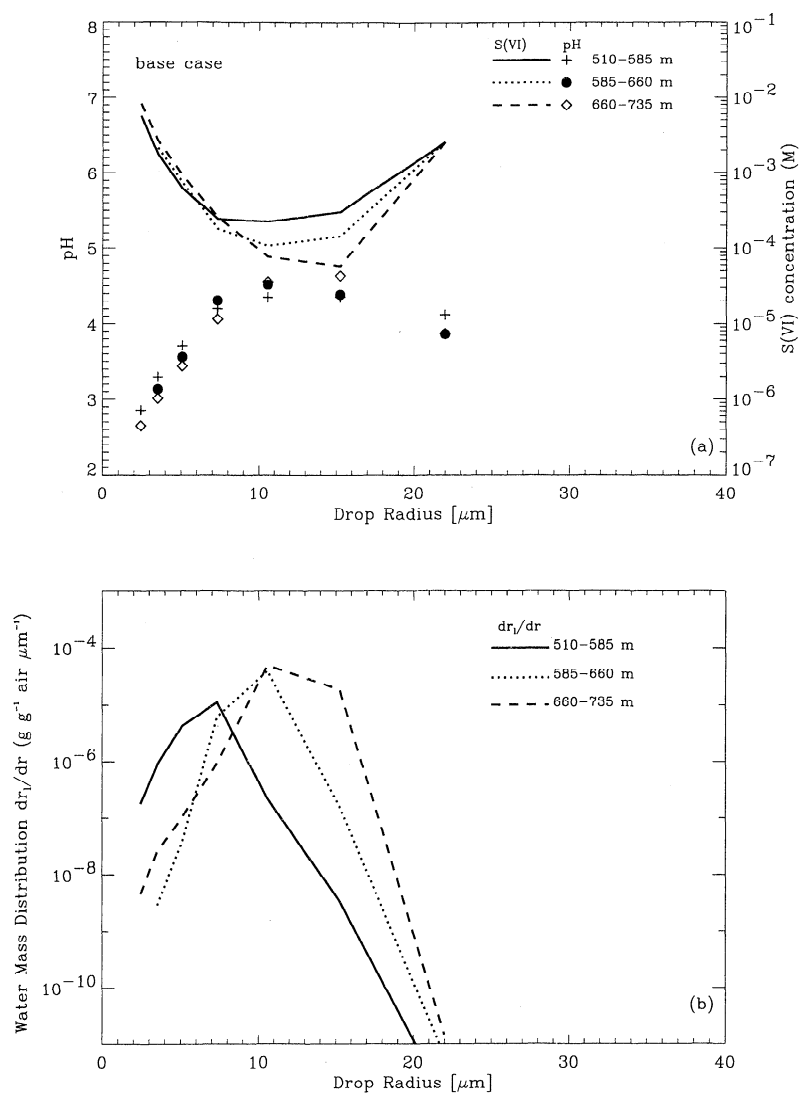
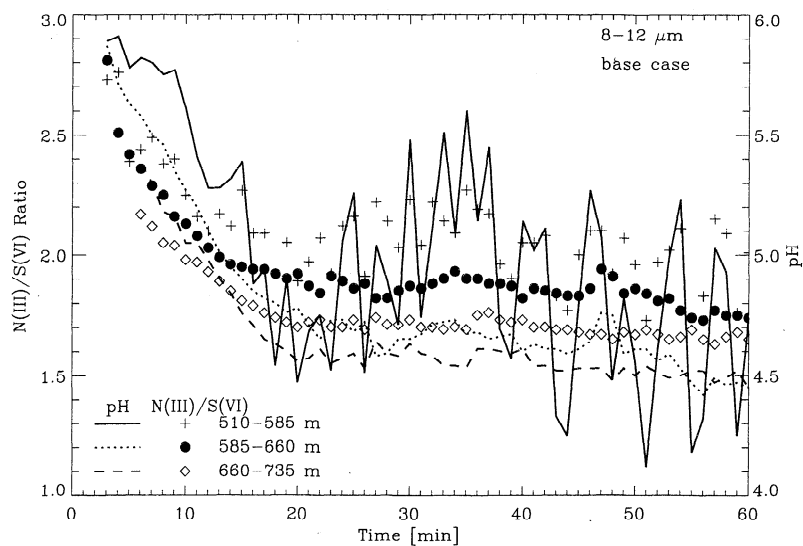**Figure 5.** As in Figure 1, but for the coupled chemistry / microphysics run for the base case.

Figure 6. Snapshots of the computed N(III) to S(VI) molar ratios and liquid water-weighted pH for the drop size range 8-12 μm for the base case. Calculations are performed at three different 75 m height intervals as indicated. The lines are for the liquid water-weighted pH, and the symbols are for the N(III) to S(VI) ratios.
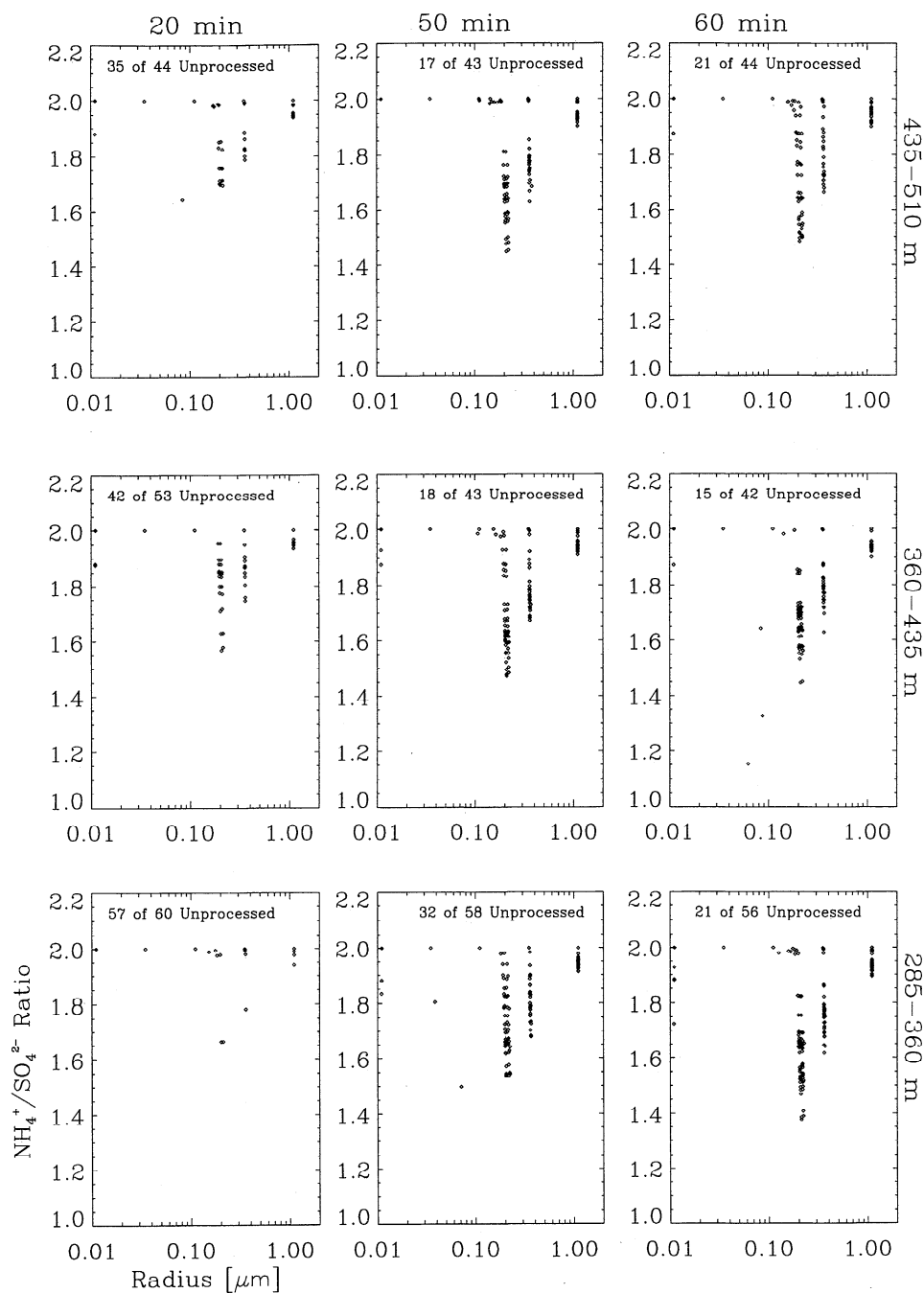
Figure 7. Snapshots of the unaveraged NH_4^+/SO_4^{2-} molar ratios in each particle size category as functions of dry particle radius at 20 min, 50 min, and 60 min, and at three different 75 m height intervals below cloud for the base case.

feature for each parcel is that the oxidation rate from the O_3 pathway is always 1 to 2 orders of magnitude larger than that from the H_2O_2 pathway for the first several minutes, but then oxidation is dominated by the H_2O_2 pathway for the rest of the in-cloud residence time, regardless of the time of second entry into the cloud. This is because the initial pH is relatively high as gaseous NH_3 dissolves into the cloud droplets, enhancing the O_3 pathway. As chemical conversion proceeds and sulfate is produced, the buffering capacity from the available NH_3 is quickly lost, pH drops, and the O_3 oxidation rate is significantly reduced. In contrast, the H_2O_2 oxidation is insensitive to pH and changes very little, except during the

entry into and exit from cloud, as the H_2O_2 is absorbed or outgassed. In the first few minutes in cloud, the H_2O_2 oxidation rate increases with time, since the timescale for the dissolved H_2O_2 to reach equilibrium with its gas phase is much longer than for O_3. The H_2O_2 oxidation rate decreases slightly with time as reagents are depleted. However, when parcels reenter the cloud for the second time, the H_2O_2 oxidation rate is immediately much higher than the O_3 pathway and remains dominant, since the available buffering agent, NH_3 gas, has already been consumed in the first cycle through cloud, as illustrated in Figure 9 for parcel 2.

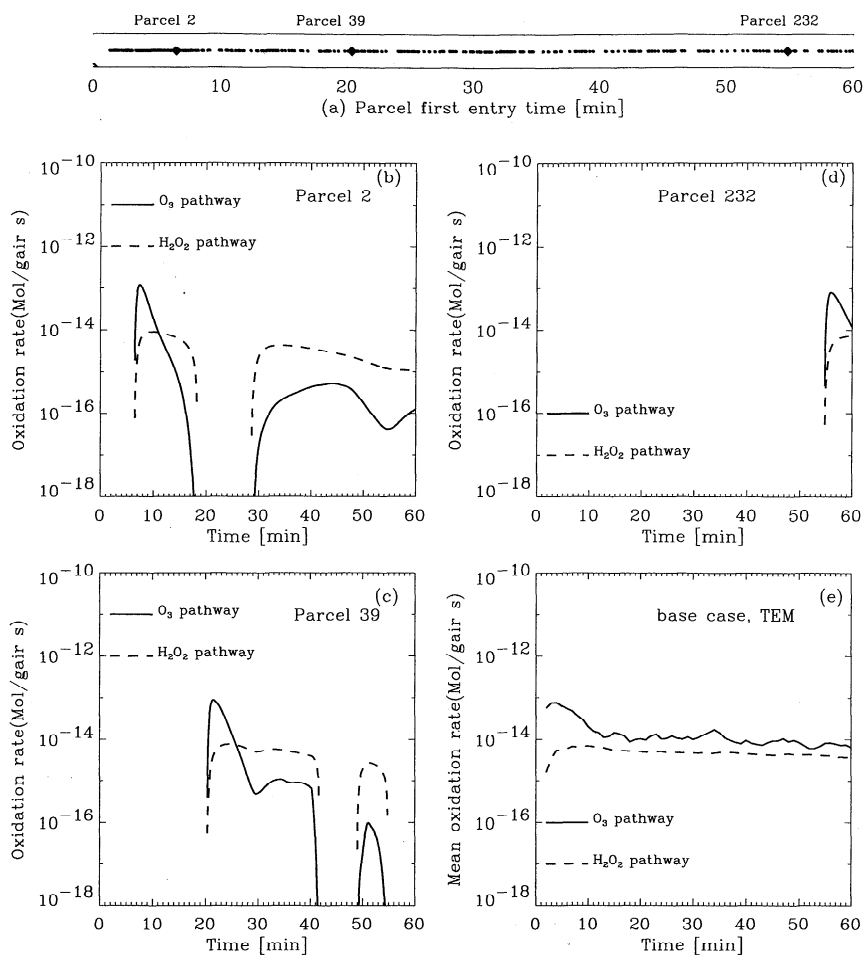Interestingly, when the oxidation rates are averaged over

Figure 8. (a) Time of first entry into cloud for each of the 500 parcels. The three diamonds indicate time of entry for parcel 2 during first 10 min, parcel 39 between 10 and 50 min, and parcel 232 during the last 10 min, respectively. Lower panels show the contribution from all drop categories to the oxidation rates via the H_2O_2 and O_3 pathways as a function of time: (b) parcel 2, (c) parcel 39, (d) parcel 232, and (e) TEM. The calculations for the TEM are averaged from 500 parcels.
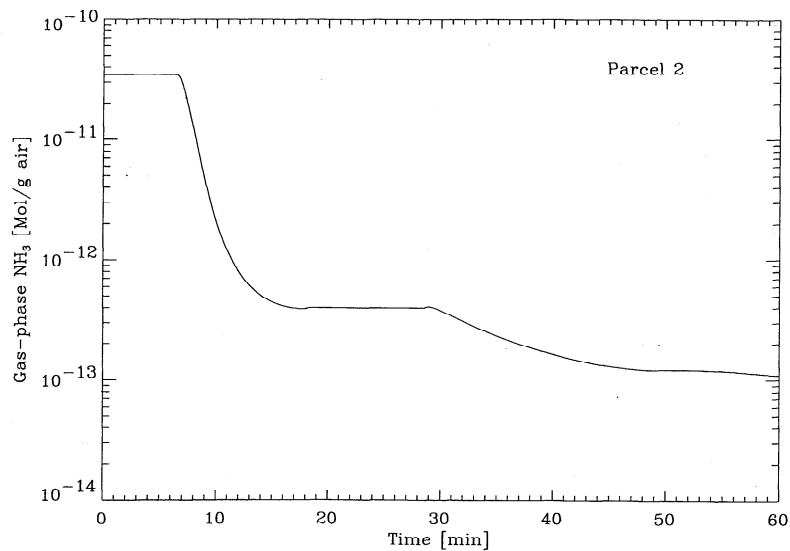

Figure 9. The depletion of gaseous NH_3 as a function of time for parcel 2.
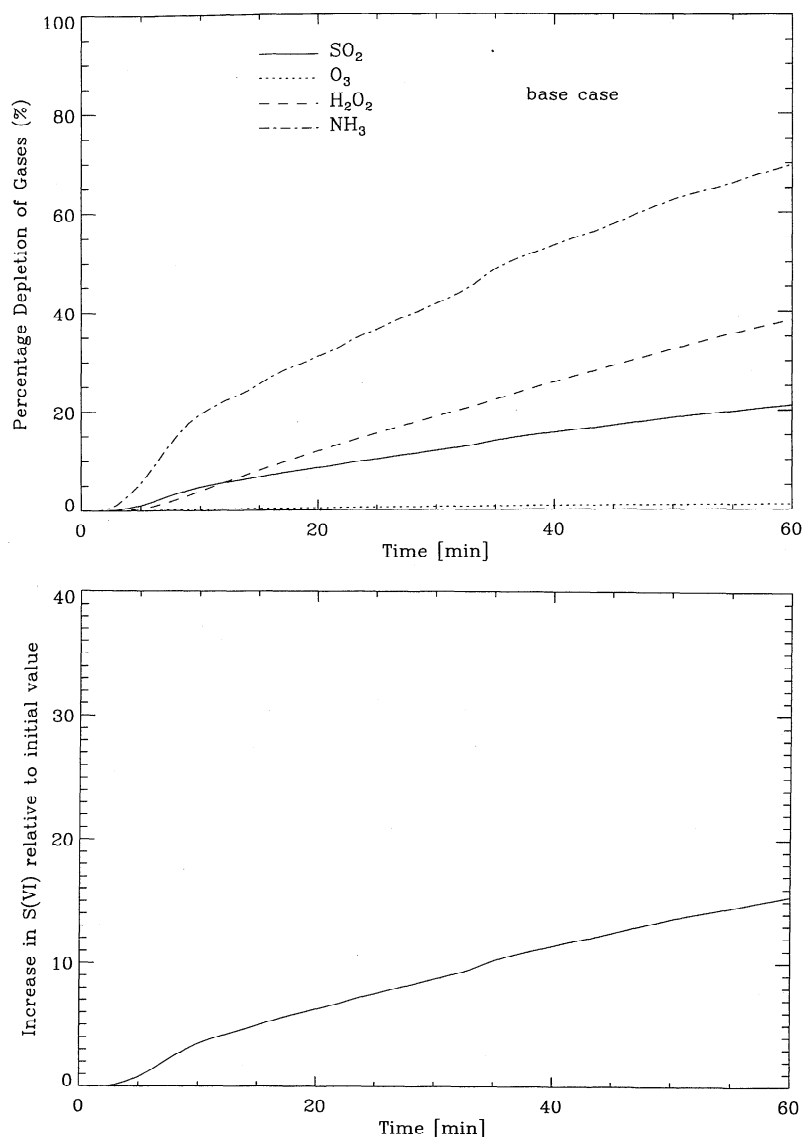
Figure 10. The percentage depletions of gaseous concentrations and increase in S(VI) relative to the initial values plotted as functions of time. Calculations are from the 500-parcel average.

all 500 parcels, the dominance of the H_2O_2 reaction is not evident. Figure 8e shows the ensemble averaged H_2O_2 and O_3 oxidation rates over time. For each pathway, we first take the sum of the contributions from each drop-size category, and then average over all the parcels in cloud at a given time. Initially, when the mean cloud water pH is still relatively high (around 5-6), the O_3 pathway is about 2 orders of magnitude larger than the H_2O_2 pathway; after 20 min, the volume-mean pH drops to around 4.5. This low cloud water pH at the gas phase concentrations selected for the base case might suggest that the O_3 oxidation is not important. However, from Figure 8e, it is seen that the averaged O_3 oxidation rate is, in fact, larger than the averaged H_2O_2 oxidation rate, although they converge to the same order of magnitude at later times. Again, this result is explained by the fact that there are almost always new parcels entering the cloud for the first time (Figure 8a) and the contributions to the O_3 oxidation from these fresh parcels are superimposed on the ones with lower O_3 oxidation rates. Thus the O_3 oxidation is important throughout the

simulation in the base case, despite the low volume mean pH over most of the simulation.

The percentage depletion of gaseous concentrations and the increase in S(VI) relative to initial values are plotted as functions of time in Figure 10. These values are calculated from the 500 parcel average, including those parcels that never enter cloud. At the end of the hour there is a 22% depletion in SO_2, 1% depletion in O_3, 39% depletion in H_2O_2, and 71% depletion in NH_3; the sulfate amount is 16 times larger than the original value for the initial CCN spectrum used here. These values and depletion patterns will vary with changes in the initial chemical fields and will, in turn, affect the total conversion rates, as discussed below.

4. Sensitivity Simulations and Discussion

To investigate the potential for stratocumulus processing to modify aerosol size spectra and drop spectra, we have performed several sensitivity tests to examine the effects of
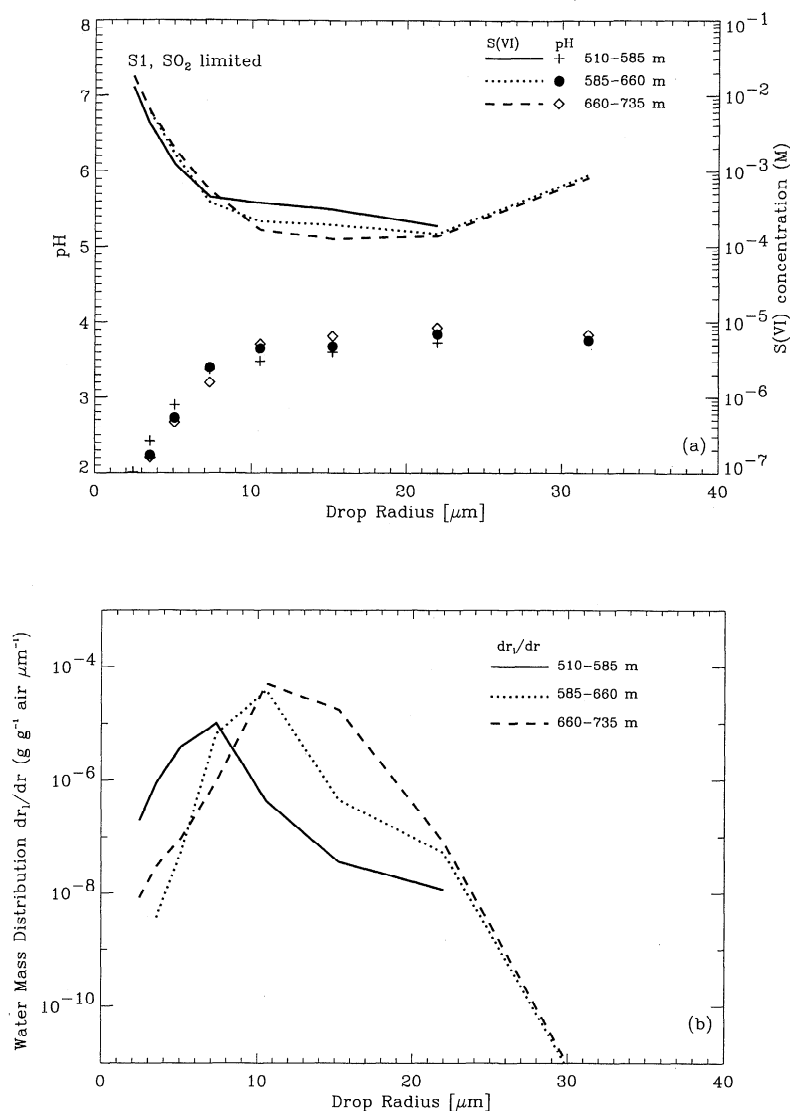
Figure 11. As in Figure 1, but for sensitivity experiment S1.

different initial chemical conditions and of different oxidation pathways on the modification of aerosol and drop spectra. To this end, we choose a SO_2 limited case (sensitivity test 1, S1), and $NH_3/SO_2 > 2$ case (sensitivity test 2, S2), to compare with the base case. An additional sensitivity test is the change in the initial CCN number concentration from 50 to 150 cm^{-3} (sensitivity test 3, S3), which affects the drop-size-dependent pH, because the drop size distribution is different.

The initial chemical and aerosol fields for the sensitivity simulations selected to demonstrate these differences are listed in Table 2. In the H_2O_2 limited case (base case), the O_3 and H_2O_2 oxidation pathways both play roles in aqueous conversion; in S1, excess H_2O_2 exists, and the H_2O_2 oxidation pathway dominates; whereas in S2 the excess NH_3 boosts the O_3 oxidation rate. The base case and S2 have a common feature in that O_3 plays a significant role in the aqueous chemistry. The overall S(IV) to S(VI) conversion in S3 is similar to that in the base case.

4.1. Effects of Varying Initial H_2O_2 Concentration on pH and Cloud Drop Spectra

We vary the initial H_2O_2 gas concentration in S1 such that it is in excess of the initial SO_2. The computed liquid water-weighted pH, mean S(VI) concentration, and mean dr_l/dr are plotted as functions of drop radius in Figure 11, which may be compared to the base case shown in Figure 5. For smaller droplets the pH dependence on drop sizes agrees qualitatively with the base case, although the pH is almost a unit lower in S1 due to more S(IV) to S(VI) conversion. However, at larger drop sizes, pH is approximately constant with size and does not show the lowering of pH at large sizes evident in Figure 5a. This effect is due to the relative abundance of larger drops, which are dilute and contribute to the higher pH and low S(VI) concentrations.

Figure 11b shows the average drop mass density dr_l/dr as functions of drop radius. A broadened cloud drop spectrum compared to that in the base case (Figure 5b) is evident, with
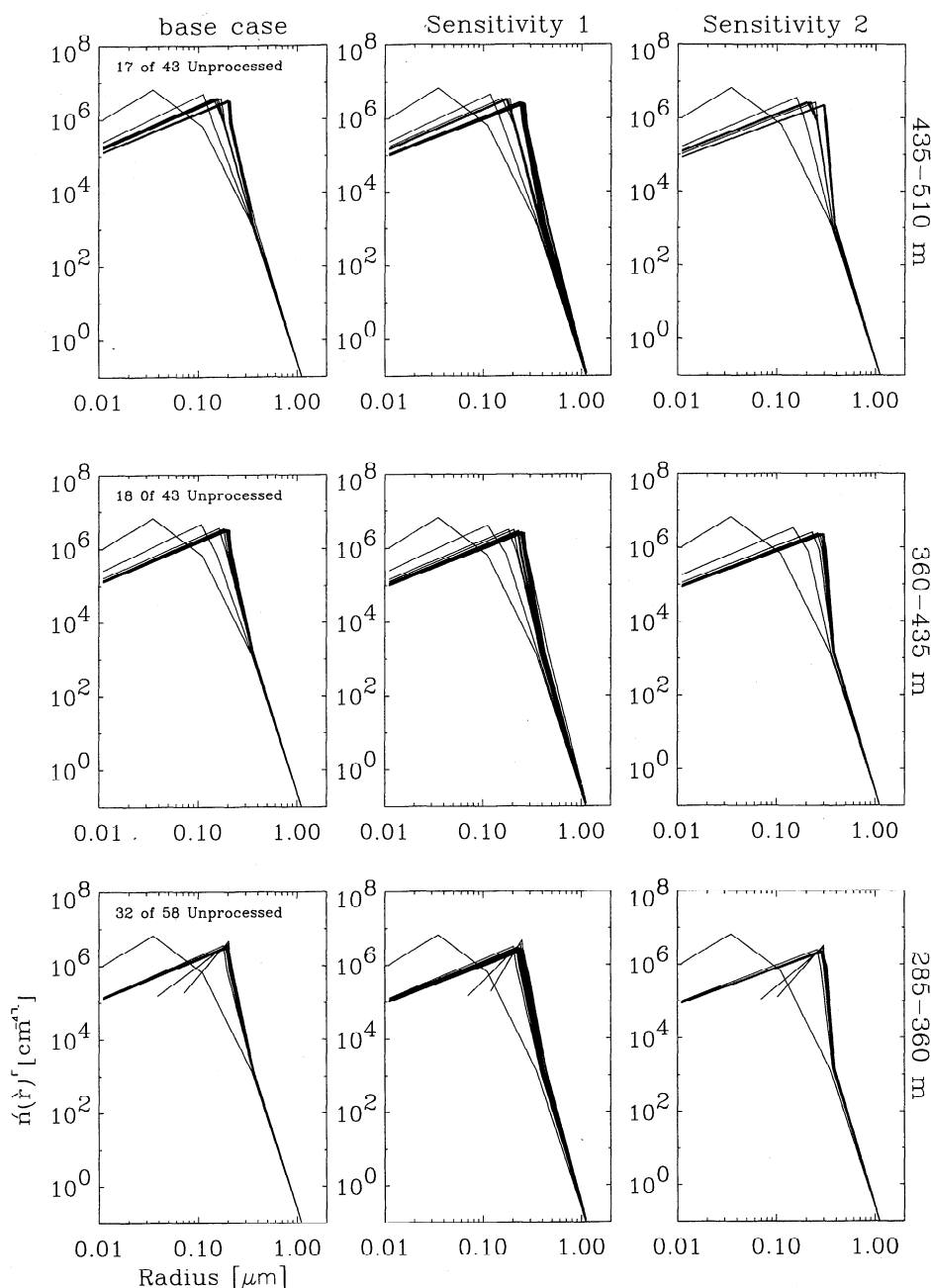
Figure 12. A comparison of the snapshots at 50 min of the unaveraged CCN size spectra on a moving mass grid at three different 75 m height intervals below cloud for the base case, S1, and S2.

significant r_l in drops greater than 20 μm in each cloudy layer. In the top two layers for S1 the number distribution for the giant cloud drops (larger than 20 μm) is greater than 0.001 mg^{-1} μm^{-1} (not shown), sufficient to play a significant role in triggering the collision − coalescence process and drizzle formation in stratocumulus clouds [*Pruppacher and Klett*, 1978; *Feingold et al.*, 1999].

To shed light on this, the unaveraged CCN spectra at three different 75 m height intervals below the cloud, at $t = 50$ min, are shown in Figure 12 for the base case, S1, and S2 (discussed below). Note that what appears to be a single unprocessed size spectrum actually consists of many

identical superimposed spectra. In S1, with excess H$_2$O$_2$ available and the S(VI) production limited only by SO$_2$ and the rate of reaction, gaseous SO$_2$ dissolves into the aqueous phase and is converted to S(VI) whenever parcels enter cloud. Because the initial H$_2$O$_2$ is increased by a factor of 8.3 in S1 compared to the base case, more SO$_2$ is converted to S(VI) after 50 min in S1, resulting in enhanced processing.

In each individual parcel the largest particles take up water first, but their ionic strength is too high initially, and little chemistry proceeds in these drops. Since the environmental gaseous NH$_3$ concentration is already very low, as these drops grow larger and the ionic strength becomes smaller, the N(III)
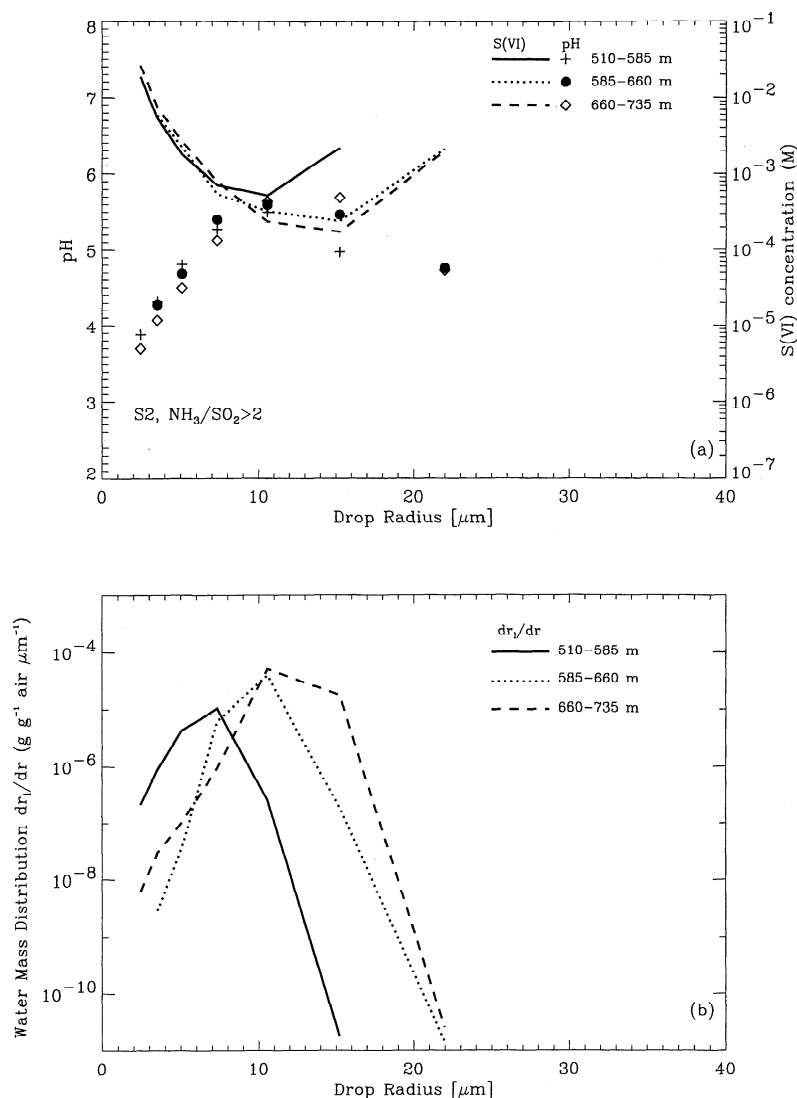
Figure 13. As in Figure 1, but for sensitivity experiment S2.

inside some larger drops is outgassed as the aqueous and gas phases equilibrate. This quickly brings down the pH values in those drops. Thus the O_3 oxidation pathway is not favored on the drops formed on larger particles, due to the strong pH dependence of that mechanism.

In S1, H_2O_2 plays a more significant role than O_3, since the H_2O_2 rate is not strongly pH dependent. The produced sulfate is thus distributed more evenly across the drop-size spectrum, which adds more sulfate mass to the large tail of the initial CCN spectrum than in the base case. This, in turn, tends to broaden the processed CCN spectrum. The broadened tail of the processed CCN spectrum in S1 allows growth of large cloud drops in each cloudy layer and contributes to the broadening of the cloud drop spectrum. These larger cloud drops are relatively dilute compared with the base case, which keeps their pH relatively high and their S(VI) concentration relatively low (Figure 11a). In the base case, with little sulfate mass added to the large tail of the initial CCN spectrum, dr_l/dr at larger drop sizes is much lower (Figure 5b).

4.2. Effects of Varying Initial NH_3 Gas Concentration on pH and Cloud Droplet Spectra

In S2 the initial gaseous NH_3 concentration is increased to 4.05 ppb, so that the initial NH_3 / SO_2 ratio is slightly greater than 2. In this case, O_3 plays a more prominent role in the aqueous chemistry due to the excess available buffering agent, NH_3 gas, and in-cloud N(III) to S(VI) ratios are maintained at a value around 2 as time elapses. The overall conversion of SO_2 for the 500 parcels ensemble is 64%, compared to 21% for the base case and 45% for S1. As in Figure 11, Figure 13 shows the mean liquid water-weighted pH, the mean S(VI) concentration, and the average drop mass spectra dr_l/dr for S2. We find that the pH dependence on drop size and the drop spectra are similar to the base case, and they are quite different than S1.

In the base case and S2 those large drops formed on larger particles experience little aqueous chemistry due to their high ionic strength, and NH_3 and SO_2 are primarily consumed in
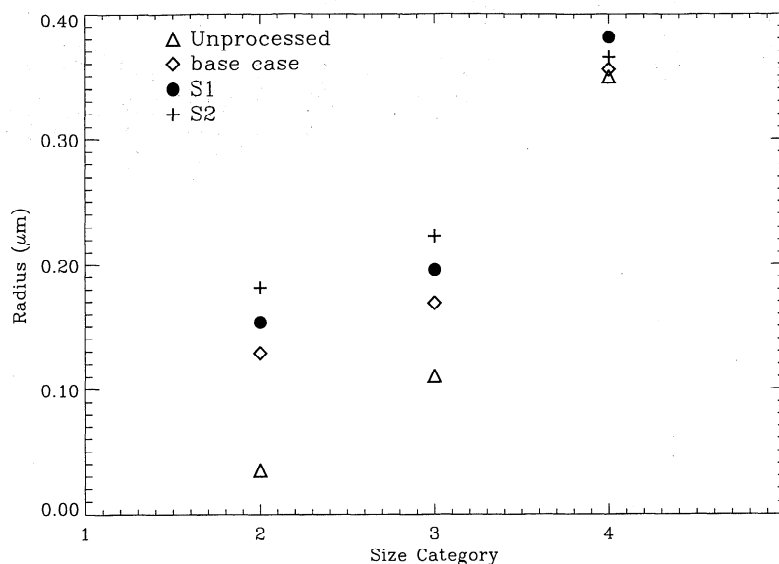
Figure 14. A comparison of the averaged dry CCN size for categories 2, 3, and 4 at 50 min for the base case, S1, and S2.

drops at the mode size of the spectrum, which have been formed on small particles. When the ionic strength in those drops formed on the largest particles is reduced, almost all gaseous SO_2 and NH_3 have already been consumed, the N(III) in the larger drops is outgassed, and their pH decreases, reducing the effectiveness of the O_3 pathway. In contrast, in S1 the H_2O_2 pathway dominates, so these pH variations do not have a pronounced effect. Conversion proceeds more evenly across the drop spectrum.

The averaged CCN radii, which have been modified by addition of mass via chemistry, are plotted against size category for the base case, S1, and S2 in Figure 14. The results pertain to values at 50 min over the layer immediately under cloud (435-510 m). Categories 1 and 5 experience little change and are not shown in the plot. Particles in categories 2 and 3 are substantially increased in size through the mass addition of S(VI) and NH_4^+, with the largest increases in S2 commensurate with the higher S(VI) production in that case. However, category 4 (initially 0.35 μm) shows maximum growth in S1, despite a lower overall S(IV) conversion than S2.

This implies that sulfate production occurs most strongly near the mode of the initial CCN spectrum in S2, since this is where most of the r_l exists and small particles reside. This translates into a stronger shift in the mode of the processed CCN spectrum toward larger sizes than in S1 (Figures 12 and 14), with less mass added onto the tail of the CCN spectrum. This strengthened CCN mode size will favor the growth of categories 2 and 3 and inhibit the growth of category 5 and produce narrow drop spectra. On the other hand, the broadened tail of the processed CCN spectrum in S1 allows growth of large cloud drops and contributes to the broadening of the cloud drop spectra. From the comparison between S1 and S2, one may conclude that the broadening of the processed CCN spectrum and cloud drop spectrum in subsequent cloud cycles will depend not only on the total

sulfate produced, but also on the distribution of the sulfate mass across the size spectrum.

4.3. Effects of Varying Initial CCN Concentration on pH and Cloud Drop Spectra

In S3 the initial CCN concentration is increased to 150 cm^{-3} with the same initial dry aerosol sizes in the five categories. As in the base case, most CCN are grown into drops, except the smallest particle size category with relatively small number concentration. With approximately the same r_l available, we would expect the mean drop radius to decrease by about $3^{1/3}$ in each cloudy layer; in the top cloudy layer, $r = 8$ μm compared to $r = 12$ μm in the base case. Although the overall S(IV) to S(VI) fractional conversion changes little, the pH dependence on drop size is affected because of the modified drop distribution. Figure 15 shows the computed volume-weighted pH, S(VI) concentration, and dr_l/dr as functions of drop radius for the last 10 min. As expected, the first pH peak has shifted to a smaller size than that in the base case, as has the U shape of the S(VI) concentration. The pH dependence on drop radius generally has a similar pattern to that in the base case.

4.4. Overall Percentage Conversion of S(IV) to S(VI): TEM Versus a Single Parcel Experiencing Mean Conditions

Here we explore further the difference between the TEM and a single parcel experiencing mean cloudy boundary layer conditions for different chemical initializations. Although stratocumulus decks are persistent for hours or even days, the relevant timescale for aqueous chemistry is the time that a typical air parcel trajectory spends in cloud. The choice of sensitivity studies is related to the relationship of the time-dependent aqueous conversion to the mean in-cloud residence time and to differences in the slopes of the time-dependent S(IV) conversion, shown in Figure 16 for the
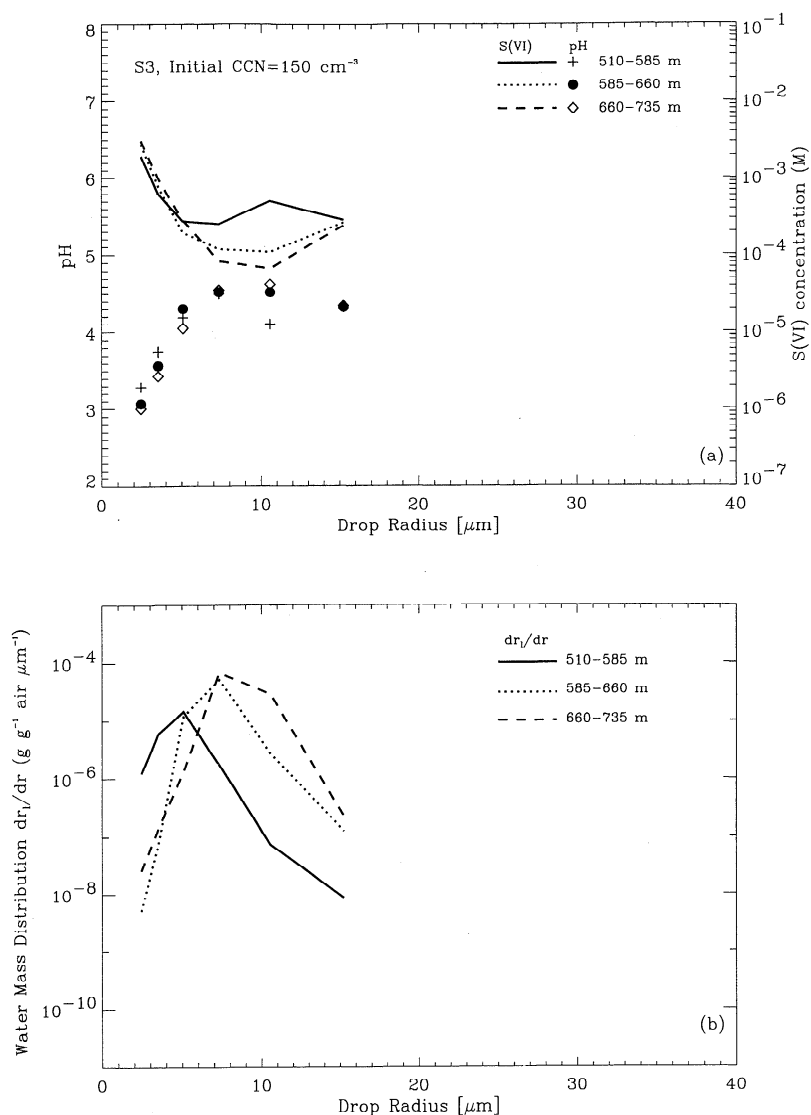
Figure 15. As in Figure 1, but for sensitivity experiment S3.

average parcel experiencing mean conditions. The mean conditions are derived from the 500 parcels and are as follows: T=280 K; mean haze and drop radii of 0.02 µm, 9.6 µm, 11 µm, 14 µm and 15.5 µm; and mean r_l = 0.18 g kg^{-1} air. In the base case the gaseous SO_2 depletion slows down after 10 min; in S1 the gaseous SO_2 depletion steadily increases; whereas in S2 the gaseous SO_2 is nearly depleted within 10 min. The base case and S2 have common features, in that O_3 plays a significant role in the aqueous chemistry, and they have similar conversion slopes. There is little difference in the S(IV) conversion in the base case and S3.

The conversion predicted from the TEM for 1 hour of cloud lifetime is illustrated in Table 3. The TEM-predicted conversion was diagnosed from the average of the percentage depletion of S(IV) in the ensemble of 500 parcels and thus accounts for interparcel variations in amount of time spent in cloud and in drop-size-, r_l-, and pH-dependent conversion rate c. It is also possible to estimate the overall conversion by performing the weighting directly [*Feingold et al.*, 1996], using

$$\bar{c} = \frac{\int_0^{1hr} c(t)f(t)dt}{\int_0^{1hr} f(t)dt} \qquad (1)$$

where $f(t)$ is the in-cloud residence time distribution, which expresses the frequency of occurrence of parcels spending time t in cloud during the course of 1 hour and can be determined by diagnosing the 500 parcels, and $c(t)$ is the time-dependent conversion rate from the mean parcel. This conversion rate cannot be easily determined without some simplifying assumptions. For example, the time-dependent conversions shown in Figure 16 are computed for the "mean parcel" conditions, which assume a constant, average r_l, the average drop-size spectrum, and a constant mean temperature. Using equation (1) and Figure 16, we computed the overall fractional conversions shown in Table 3; they are seen to be similar to those derived from the full TEM.

If τ_c, the mean in-cloud residence time, is known, the overall conversion may be estimated from the conversion that
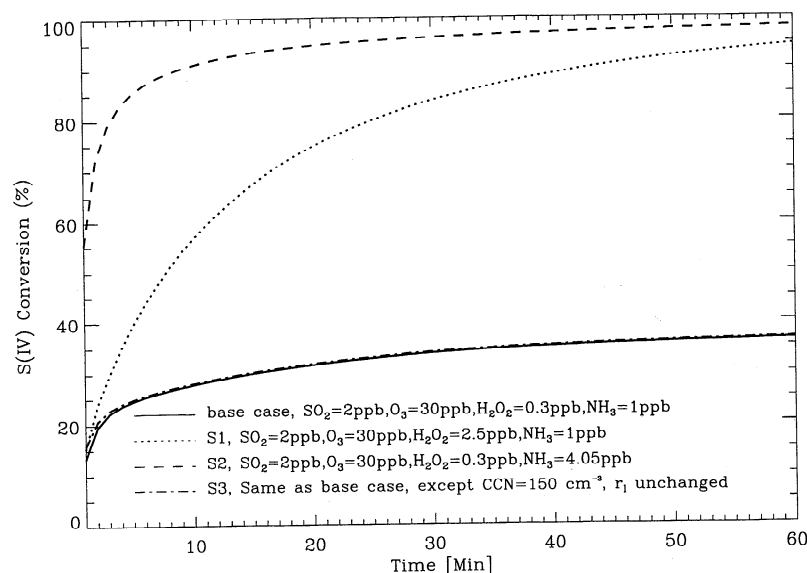
Figure 16. The fractional conversion of S(IV) from a single parcel experiencing mean conditions for the base case and sensitivity runs. Solid line is base case, dotted line is S1, dashed line is S2, and dash-dotted line is S3.

occurs over this time. Thus τ_c can be computed from the TEM statistics using

$$\tau_c = \frac{\int_0^{1hr} tf(t)dt}{\int_0^{1hr} f(t)dt}. \qquad (2)$$

About 26% of the 500 parcels never enter cloud during the 1 hour simulation time and therefore have no conversion occurring in them. The remainder of the parcels have the probability distribution function (PDF) of in-cloud residence time shown in Figure 17, for which $\tau_c = 18$ min. For those parcels the fractional conversion $\bar{c}_{in-cloud}$ inferred from τ_c and Figure 16 is

$$\bar{c}_{in-cloud} = c(\tau_c), \qquad (3)$$

where $c(\tau_c)$ is the percent conversion at time τ_c for the average parcel. The overall conversion occurring in the boundary layer is then

$$\bar{c} = 0.74\bar{c}_{in-cloud} + 0.26c(0) = 0.74\bar{c}_{in-cloud} \qquad (4)$$

where the zero contribution from parcels that have never cycled through cloud has been accounted for. The estimates derived using equation (4) are shown in Table 3.

From Table 3, the PDF-weighted fractional conversion (equation (1)) is closer to the TEM results, with 7 - 11% errors, while estimates using only the mean residence time (equation (4)) can give errors of 9 - 19%. Note that the steadily increasing conversion slope for S1 (compared to S2, S3, and the base case, for which the conversion flattens before or near the mean in-cloud residence time) results in the largest error between the two approximate methods and the TEM. We anticipate that the differences will get larger for cases in which the mean in-cloud residence time for 500 parcels is shorter than 10 min, where the conversion rates are faster.

As discussed in detail by *Gurciullo and Pandis* [1997], bulk cloud water reaction rates are generally lower than those computed using size-resolved chemistry, as done in this work, and the overall conversions predicted by the two methods can differ by factors of more than 10. The errors introduced by computing overall conversion assuming a mean in-cloud residence time must be considered in addition to the differences between size-resolved and bulk cloud water chemistry. The overall error will depend upon the composition of the aerosol spectrum, the pH dependence of the aqueous pathways, and the relationships of the in-cloud residence time distribution to the time-dependent conversion rates.

Table 3. Overall S(IV) to S(VI) Conversion Computed Via Various Methods as Discussed in Text

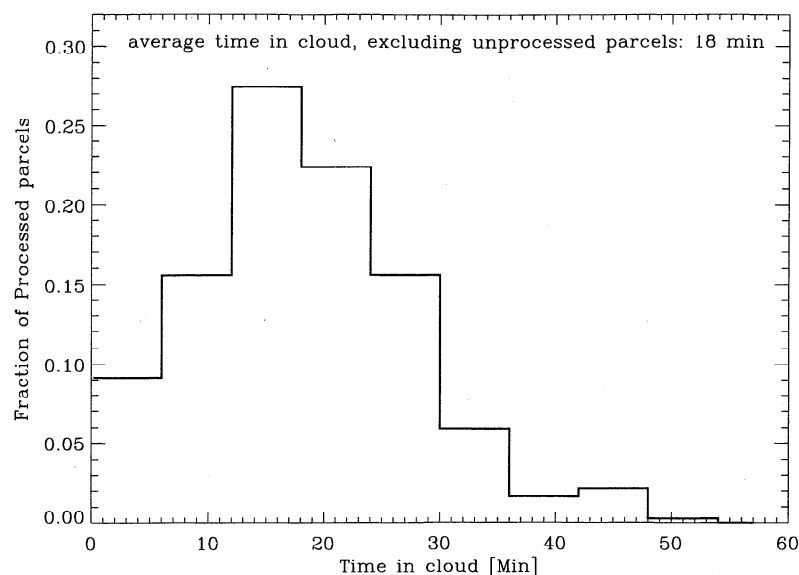|	TEM	Single Parcel (1)		Single Parcel (4)	
	% Conversion	% Conversion	% Difference From TEM	% Conversion	% Difference From TEM
Base case	21.9	22.5	7	23.2	10
Sensitivity test 1	45.3	50.5	11	54.1	19
Sensitivity test 2	64.3	68.9	7	70.2	9
Sensitivity test 3	21.1	22.8	8	23.5	11

Figure 17. The probability distribution function (PDF) of in-cloud residence time for those parcels entering cloud during the 1 hour simulation.

4.5. Possible Implications of the Neglect of Mixing on the Degree of Processing

In our current work there is no communication between parcels. In a general sense, mixing acts to homogenize the air in gases and CCN. It might be argued that if neglect of mixing results in approximately equal numbers of parcels that are enriched in gases and parcels that are depleted in gases that in the mean, processing would be similar to that resulting from all parcels having a more homogenized state. However, the impact of neglect of mixing will also depend on the subsequent trajectories of the individual parcels (time in cloud, liquid water content), as well as on the nonlinearity of the processing with respect to gas concentrations and CCN distribution. The latter is probably case dependent (as suggested by Figure 16). One must also take into account that parcels that never enter cloud represent a constant source of replenishment of gases and unprocessed CCN, which would allow stronger processing were mixing to be treated.

Let us consider a number of simple scenarios that might assist in evaluating the implications for processing of aerosol and gases. (1) Consider two parcels that enter and exit cloud at similar times and experience similar degrees of gaseous depletion and CCN modification. In such a case, the neglect of exchanging information between these parcels will have little impact. (2) If a parcel that has been depleted in gases during a recent sojourn into cloud (parcel A) encounters one that is undepleted because it has never entered cloud (parcel B), the impact of no mixing is difficult to assess. On the one hand, a mixing event between these parcels would deplete B in gases prior to its entrance into cloud and therefore limit processing occurring in B while it is in cloud. It would also supply B with a somewhat different CCN distribution from its initial state. The impact on A in this scenario would be of opposite trend because communication with B would replenish some of those gases and aerosol so that if it returned to cloud (as is common in this trajectory set) it would experience enhanced processing (relative to the case where it did not communicate

with B). Considering these two scenarios suggests that neglect of mixing does not represent either an upper bound nor a lower bound on processing. However, it is clear that other scenarios are possible, especially when considering all 500 parcels and their many possible mixing scenarios.

Results presented in section 3.4 for the base case indicated that the dominant oxidation pathway is via O_3, despite the low volume-mean pH in each cloudy layer that might indicate that H_2O_2 is the dominant pathway. The explanation for this resided in the high concentrations of NH_3 present in parcels entering cloud for the first time, and the associated high pH values that boosted the O_3 oxidation rates. The neglect of interparcel mixing may have some impact on this result. If parcels entering cloud for the first time are depleted in NH_3 because of a mixing event with a parcel that had previously resided in cloud, the result would be a lower oxidation rate via the O_3 pathway. On the other hand, had mixing been represented, such a parcel would also enter cloud with lower H_2O_2 concentrations which would lower the H_2O_2 oxidation rates. It is difficult to assess whether the inclusion of mixing would reverse the relative importance of the two pathways, but it is likely that this result would be case dependent. Inclusion of interparcel mixing processes and examination of their effect on model results is a very interesting problem that is worthy of pursuit in a further study.

5. Summary and Conclusion

In this paper, we have utilized the TEM to simulate coupled aqueous chemistry and cloud microphysics and have investigated the effects of variations in the initial chemical fields and initial aerosol number concentration on chemical heterogeneity across the cloud drop sizes, broadening of the CCN and drop spectra, and differences in the overall fractional conversion between the TEM and a single parcel experiencing mean conditions. The TEM offers a more representative method of describing the stratocumulus processing of aerosol

and gases than does a single parcel model. A single parcel experiencing mean conditions overestimates the fractional conversion of S(IV) compared to the TEM results. Different shapes of the time-dependent conversion and its convolution with the residence time distribution will affect the magnitudes of the difference between a single mean parcel and the TEM, with the steadily increasing conversion with time inducing the largest error. Fractional conversions estimated using the distribution of in-cloud residence times convoluted with the time-dependent conversion for an average parcel give results within about 10% of those predicted by the full TEM.

For this boundary layer initialized with the base case chemical fields, there are frequent intrusions of NH_3-rich air into the cloud, which result in brief, but strong oxidation of SO_2 via the O_3 pathway, before the pH drops too low. Therefore, on average, the O_3 oxidation rate is larger than the H_2O_2 oxidation rate, whereas the volume-mean pH might suggest that H_2O_2 oxidation is the dominant conversion mechanism. This result is expected to be case dependent and may also depend on the neglect of interparcel mixing in the TEM.

A combination of variable growth histories and aqueous chemistry contributes to the broadening of the drop-size distribution. A broadened CCN spectrum that is created by aqueous chemistry in a previous cloud cycle reenters the cloud and produces a broadened drop spectrum, but the magnitude of the broadening depends on the initial chemical conditions. The H_2O_2 oxidation pathway adds sulfate mass evenly and continuously across the drop sizes, while the O_3 oxidation pathway adds sulfate mass near the mode of the CCN spectrum over a relatively short time. The different behaviors of the O_3 oxidation and H_2O_2 oxidation, in turn, affect the pH dependence on the drop sizes and the magnitude of the broadening of the cloud drop spectrum. In cases where more mass is added onto the large tail of the initial CCN spectrum, the broadening of the drop spectrum is most evident and may even trigger the collision – coalescence process and drizzle formation.

References

Betts, A. K., and R. Boers, A cloudiness transition in a marine boundary layer, *J. Atmos. Sci.*, *47*, 1480-1497, 1990.

Bower, K. N., and T. W. Choularton, Cloud processing of the cloud condensation nucleus spectrum and its climatological consequences, *Q. J. R. Meteorol. Soc.*, *119*, 655-679, 1993.

Brown, P. N., G. D. Byrne, and A. C. Hindmarsh, VODE: A variable coefficient ODE solver, *SIAM J. Sci. Stat. Comput.*, *10*, 1038-1051, 1989.

Chen, J. P., Theory of deliquescence and modified Köhler curves, *J. Atmos. Sci.*, *51*, 3505-3516, 1994.

Daum, P. H., T. J. Kelly, S. E. Schwartz, and L. Newman, Measurements of the chemical composition of stratiform clouds, *Atmos. Environ.*, *18*, 2671-2684, 1984.

Feingold, G., and A. J. Heymsfield, Parameterizations of condensational growth of droplets for use in general circulation models, *J. Atmos. Sci.*, *49*, 2325-2342, 1992.

Feingold, G., S. M. Kreidenweis, B. Stevens, and W. R. Cotton, Numerical simulations of stratocumulus processing of cloud condensation nuclei through collision-coalescence, *J. Geophys. Res.*, *101*, 21391-21402, 1996.

Feingold, G., S. M. Kreidenweis, and Y. Zhang, Stratocumulus processing of gases and cloud condensation nuclei, 1, Trajectory ensemble model, *J. Geophys. Res.*, *103*, 19527-19542, 1998.

Feingold, G., W. R. Cotton, S. M. Kreidenweis, and J. T. Davis, Impact of giant cloud condensation nuclei on drizzle formation in marine stratocumulus, *J. Atmos. Sci.*, in press, 1999.

Gurciullo, C. S. and S. N. Pandis, Effect of composition variations in cloud droplet populations on aqueous-phase chemistry, *J. Geophys. Res.*, *102*, 9375-9385, 1997.

Hales, J. M., and D. R. Drewes, Solubility of ammonia in water at low concentrations, *Atmos. Environ.*, *13*, 1133-1147, 1979.

Hegg, D. A., and T. V. Larson, The effects of microphysical parameterization on model predictions of sulfate production in clouds, *Tellus, Ser. B.*, *42*, 272-284, 1990.

Hegg, D. A., R. Majeed, P. F. Yuen, M. B. Baker, and T. V. Larson, The impacts of SO_2 oxidation in cloud drops and in haze particles on aerosol light scattering and CCN activity, *Geophys. Res. Lett.*, *23*, 2613-2616, 1996.

Hoffmann, M. R., and J. G. Calvert, Chemical transformation modules for eulerian acid deposition models, vol. 2, The aqueous-phase chemistry, *Rep. EPA/600/3-85/036*, U.S. Environ. Prot. Agency, Research Triangle Park, N.C., 1985.

Hoppel, W. A., and G. M. Frick, Submicron aerosol size distributions measured over the tropical and south Pacific, *Atmos. Environ.*, *24A*, 645-659, 1990.

Hoppel, W. A., G. M. Frick, J. W. Fitzgerald, and R. E. Larson, Marine boundary layer measurements of new particle formation and the effects nonprecipitating clouds have on aerosol size distribution, *J. Geophys. Res.*, *99*, 14443-14459, 1994.

Korolev, A. V., The influence of supersaturation fluctuations on droplet size spectra formulation, *J. Atmos. Sci.*, *20*, 3620-3634, 1995.

Kozac-Channing, L. F., and G. R. Heltz, Solubility of ozone in aqueous solutions of 0-0.6 M ionic strength at 5-30C, *Environ. Sci. Technol.*, *17*, 145-149, 1983.

Lelieveld, J. and P. J. Crutzen, The role of clouds in tropospheric photochemistry, *J. Atmos. Chem.*, *12*, 229-267, 1991.

Lind, J. A., and G. L. Kok, Henry's law determinations for aqueous solutions of hydrogen peroxide, methylhydroperoxide, and peroxyacetic acid, *J. Geophys. Res.*, *91*, 7889-7895, 1986.

Macdonald, A. M., K. G. Anlauf, C. M. Banic, W. R. Leaitch, and H. A. Wiebe, Airborne measurements of aqueous and gaseous hydrogen peroxide during spring and summer in Ontario, Canada, *J. Geophys. Res.*, *100*, 7253-7262, 1995.

Mazin, I. P., The stochastic condensation and its effect on the formation of cloud droplet size distribution, in *Proceedings of the International Conference on Cloud Physics, Toronto, Canada*, pp. 67-71, 1968.

Müller, F., and G. Mauersberger, Case study on the interaction of size dependent multiphase chemistry and detailed microphysics, *Atmos. Res.*, *32*, 273-288, 1994.

Nakajima, T., M. D. King, J. D. Spinhirne, and L. F. Radke, Determination of the optical thickness and effective particle radius of clouds from reflected solar radiation measurements, 2, Marine stratocumulus observations, *J. Atmos. Sci.*, *48*, 728-750, 1991.

Noone, K. J., R. J. Charlson, D. S. Covert, J. A. Ogren, and J. Heintzenberg, Cloud droplets: Solute concentration is size dependent, *J. Geophys. Res.*, *93*, 9477-9482, 1988.

Pandis, S. N., and J. H. Seinfeld, Sensitivity analysis of a chemical mechanism for aqueous-phase atmospheric chemistry, *J. Geophys. Res.*, *94*, 1105-1126, 1989.

Pandis, S. N., J. H. Seinfeld, and C. Pilinis, Chemical composition differences in fog and cloud droplets of different sizes, *Atmos. Environ.*, *24A*, 1957-1969, 1990.

Perrin, D. D., *Ionization Constants of Inorganic Acids and Bases in Aqueous Solution*, 2nd ed., 180 pp., Pergamon, Tarrytown, N.Y., 1982.

Pruppacher, H. R. and J. D. Klett, *Microphysics of Clouds and Precipitation*, 714 pp., D. Reidel, Norwell, Mass., 1978.

Randall, D. A., J. A. Coakley Jr., C. W. Fairall, R. A. Kropfli, and D. H. Lenschow, Outlook for research on subtropical marine stratiform clouds, *Bull. Am. Meteorol. Soc.*, *65*, 1290-1301, 1984.

Roelofs, G. J. H., Drop size dependent sulfate distribution in a growing cloud, *J. Atmos. Chem.*, *14*, 109-118, 1992.

Sangster, J., and F. Lenzi, On the choice of methods for the prediction of the water-activity and activity coefficient for multicomponent aqueous solutions, *Can. J. Chem. Eng.*, *52*, 392-396, 1974.

Seinfeld, J. H., *Atmospheric Chemistry and Physics of Air Pollution*, 738 pp., John Wiley, New York, 738 pp., 1986.

Slingo, A., Sensitivity of the Earth's radiation budget to changes in low clouds, *Nature*, *343*, 49-51, 1990.

Smith, R. M., and A. E. Martell, *Critical Stability Constants,* vol. 4, *Inorganic Complexes,* 257 pp., Plenum, New York, 1976.

Stevens, B., G. Feingold, W. R. Cotton, and R. L. Walko, Elements of the microphysical structure of numerically simulated stratocumulus, *J. Atmos. Sci.,* *53,* 980-1006, 1996.

Tang, I. N., and H. R. Munkelwitz, Water activities, densities, and refractive indices of aqueous sulfates and sodium nitrate droplets of atmospheric importance, *J. Geophys. Res.,* *99,* 18801-18808, 1994.

Twohy, C. H., P. H. Austin, and R. J. Charlson, Chemical consequences of the initial diffusional growth of cloud droplets: A clean marine case, *Tellus, Ser. B., 41,* 51-60, 1989.

G. Feingold, Cooperative Institute for Research in the Atmosphere / NOAA, Environmental Technology Laboratory, 325 Broadway, Boulder, CO 80303.

S. M. Kreidenweis, Department of Atmospheric Science, Colorado State University, Fort Collins, CO 80523. (soniak@aerosol.atmos. colostate.edu)

Y. Zhang, Climate Modeling Section, CGD, National Center for Atmospheric Research, P.O. Box 3000, Boulder, CO 80307.